Preliminary Investigation of Respiratory Self-Gating for Free-Breathing Segmented Cine MRI

Andrew C. Larson,[1,2*] Peter Kellman,[3] Andrew Arai,[3] Glenn A. Hirsch,[3] Elliot McVeigh,[3] Debiao Li,[1,2] and Orlando P. Simonetti[2,4]

Segmented cine MRI generally requires breath-holding, which can be problematic for many patients. Navigator echo techniques, particularly successful for free-breathing coronary MRA, are incompatible with the acquisition strategies and SSFP pulse sequences commonly used for cine MRI. The purpose of this work is to introduce a new self-gating technique deriving respiratory gating information directly from the raw imaging data acquired for segmented cine MRI. The respiratory self-gating technique uses interleaved radial *k*-space sampling to provide low-resolution images in real time during the free-breathing acquisition that are compared to target expiration images. Only the raw data-producing images with high correlation to the target images are included in the final high-resolution reconstruction. The self-gating technique produced cine series with no significant differences in quantitative image sharpness to series produced using comparable breath-held techniques. Because of the difficulties associated with breath-holding, the respiratory self-gating technique represents an important practical advance for cardiac MRI. Magn Reson Med 53:159–168, 2005. Published 2004 Wiley-Liss, Inc.†

Key words: CMR; gating; triggering; navigator; cine

INTRODUCTION

Cardiac magnetic resonance imaging (CMR) generally requires data acquisition during a breath-hold to minimize respiratory motion artifacts. Except in the case of single-shot imaging, CMR images are typically reconstructed from data acquired in a segmented fashion over a number of cardiac cycles during a single breath-hold. In the clinical setting, many patients have difficulty performing the necessary breath-holds to allow the use of segmented acquisition strategies. Severely ill, incapacitated, or uncooperative patients often cannot perform voluntary breath-holds. Although real-time or single-shot imaging strategies may eliminate the need for breath-holding, segmented acquisitions can provide higher spatial resolution, temporal resolution, and signal-to-noise ratio (SNR).

Respiratory gating approaches for free-breathing MRI were initially developed for imaging of the chest and abdomen and incorporated the use of pneumatic bellows signals for either gating (1) or reordering of phase-encoding steps (2) to minimize motion artifacts. Bellows respiratory gating strategies have recently been successfully applied to free-breathing segmented cardiac cine applications (3). However, gating strategies utilizing such approaches may be ineffective if the chest wall position varies relative to the heart position over multiple respiratory cycles. Ideally, gating technique for free-breathing CMR should be based on changes in heart position relative to respiration.

Most recently developed free-breathing imaging approaches involve the interleaved acquisition of navigator (NAV) echoes to monitor diaphragm position (4). The NAV respiratory gating information is used to accept or reject acquired image data (5,6) and prospectively modify slab position (7). NAV respiratory gating techniques have allowed significant SNR and spatial resolution improvements for coronary MRA. NAV techniques have generally been applied in CMR strategies involving image acquisition during only a short sampling window within each cardiac cycle. For these strategies, a single NAV echo is typically acquired immediately prior to the image acquisition window. Only a short time period elapses between the acquisition of the NAV echo and the acquisition of imaging data. However, in cine acquisitions, imaging data are acquired throughout the cardiac cycle and therefore a single NAV echo acquisition during each cardiac cycle is insufficient for respiratory gating. Potentially, the acquisition of additional NAV gating echoes could be interspersed with the acquisition of imaging data throughout the cardiac cycle. However, such an approach would significantly decrease sampling efficiency by halting the acquisition of imaging data for short time intervals during each cardiac cycle to acquire the NAV echoes. Furthermore, such an approach would be less compatible with conventional SSFP cine imaging sequences (8) that require constant RF excitation to maintain the magnetization in steady state.

Ideally, to optimize imaging efficiency and avoid interrupting the acquisition to sample separate gating signals, the respiratory gating information for SSFP cine imaging applications should be derived from the same data acquired for image reconstruction. We have recently demonstrated that a cardiac gating signal can be successfully derived from the raw imaging data (9). It will be shown in this work that the same basic principal of "self-gating" can be used to derive a respiratory motion signal for free-breathing cine MRI.

Hardy et al. and Sussman et al. recently described such strategies for adaptive free-breathing 2D coronary MRA (10–12). The techniques of Hardy et al. involved repeatedly acquiring images in real time using an interleaved-

[1]Department of Biomedical Engineering, NorthWestern University, Chicago, Illinois.

[2]Department of Radiology, Northwestern University, Chicago, Illinois.

[3]Laboratory of Cardiac Energetics, NHLBI, National Institutes of Health, DHHS, Bethesda, Maryland.

[4]Siemens Medical Solutions, Malvern, Pennsylvania.

*Correspondence to: Andrew C. Larson, Northwestern University, Department of Radiology, 448 E. Ontario Suite 700, Chicago, IL 60611. E-mail: alarson@radiology.northwestern.edu

Received 16 April 2004; revised 20 July 2004; accepted 16 August 2004

DOI 10.1002/mrm.20331

Published online in Wiley InterScience (www.interscience.wiley.com).

spiral pulse sequence with one of four separate subtrajectories. Region-of-interest (ROI) cross-correlation provided information regarding whether a particular interleave was acquired with the tissue at the same spatial position as a reference image containing the desired vessel. The separate interleaves with corresponding images exhibiting sufficient correlation to the reference image were combined for a high-resolution image reconstruction. The technique of Sussman et al. involved repeatedly acquiring *k*-space interleaves with a variable density spiral sequence while reconstructing low-resolution images from the inner spiral in real time for correlation comparison to a previously acquired template image within a chosen ROI. High-resolution images were reconstructed from those full interleaves resulting in inner-spiral images with sufficient correlation to be considered identical to the template.

The method we propose for free-breathing cine MRI involves extending this gating approach based on image correlation to multiple cardiac phase cine imaging while using radial *k*-space sampling and SSFP acquisition techniques (13). With an interleaved radial *k*-space sampling scheme, subsets of sequentially acquired views can be combined to produce low-resolution gating images in real time. The 2D correlation coefficient can be computed between a gating image and a target image previously acquired at a similar cardiac phase and the desired respiratory cycle position. Ultimately, this correlation coefficient can be used to determine whether the views included in the reconstruction of a low-resolution gating image should be included in the final high-resolution reconstruction.

The purpose of this work is to introduce this new free-breathing respiratory self-gated cine MRI technique and investigate its potential in a study of normal volunteer subjects. The results obtained using free-breathing respiratory self-gated cine are compared to free-breathing *k*-space averaging techniques as well as conventional breath-hold cine techniques.

MATERIALS AND METHODS

Radial TrueFISP Acquisition and Image Reconstruction

The 2D radial TrueFISP sequence was identical to that utilized for a previously described cardiac self-gating implementation (9). Image acquisition was preceded by the application of an $\alpha/2$ RF pulse (14) followed by 400 additional dummy RF pulses (for approximately 1.2 s) to bring the magnetization to steady state prior to readout of imaging data. Imaging parameters included a 1-kHz/pixel bandwidth, 55° flip angle, 192 readout samples, 6-mm slice thickness, 300 × 300 mm^2 isotropic in-plane FOV (1.6 × 1.6 mm^2 in-plane voxel size), 40 views/segment (VPS), 160 total views/image, and symmetric echo sampling (TR/TE = 3.0/1.5 ms). All imaging experiments were performed on a Siemens 1.5-T Magnetom Sonata scanner (Siemens Medical Solutions, Erlangen, Germany) with a two-channel quadrature array coil and a six-channel spine array (typically only one of these channels were selected for use based on orientation).

A regridding reconstruction algorithm incorporating a 3 × 3 Kaisser–Bessel kernel function (15) and Ram–Lak density compensation weighting (16) was used for image reconstruction. Reconstruction time was minimized by precomputing the kernel and density compensation values needed for all sampled *k*-space data points and storing this information in a look-up table for repeated reference while regridding (17). Magnitude images reconstructed from each coil were combined using a self-weighting root sum of squares technique (18).

Each 40-view segment was acquired in an interleaved fashion such that subsets of 20 sequentially acquired views spanned roughly 180° in *k*-space. During each free-breathing scan, low-resolution images, $I(x,y)$, were reconstructed in real time at 16 frames/s, including 40 views/image (factor-of-2 view-sharing) and using only the center 80 of 192 readout points acquired for each view (3.75 × 3.75 mm^2 in-plane voxel size). These images were reconstructed at less than half of the spatial resolution provided by the full 192 sample readout to limit the amount of streak artifacts resulting from the 40-view image reconstruction.

The physiologic monitoring unit of the Sonata scanner (optical three-lead ECG recorder with 400-Hz R-wave detection processor) provided R-wave trigger time stamps with each *k*-space readout. These time stamps were representative of the time interval between the sampling of a *k*-space readout and the most recently detected R-wave. Along with each low-resolution image was stored the ECG trigger time stamp accompanying the 21st *k*-space readout, which represented the temporal center of each particular image.

No custom computing hardware was utilized for this work. All image reconstruction algorithms and prospective feedback controls were implemented within the existing software development environment of the Magnetom Sonata scanner.

Derivation of Cardiac Phase Dependent Respiratory Target Images

Prior to the respiratory self-gated scan, single-shot TrueFISP localization images (Cartesian *k*-space sampling) were acquired using imaging parameters of TR/TE = 2.8/1.4 ms, 360 × 288 mm^2 FOV, 6-mm slice thickness, 128 × 83 matrix size, 2.8 × 3.5 mm^2 in-plane voxel size during a single heartbeat breath-hold. From these localization images, a square ROI mask, from 50 × 50 to 100 × 100 mm^2, was chosen to include either the septum and left ventricle apex in long axis orientations or the septum and posterior right ventricle insertion position in short axis orientations. The ROI size was limited to reduce subsequent correlation coefficient computation times.

Each self-gated acquisition was immediately preceded by a 20-s free-breathing "target-acquisition" (TA) period (Fig. 1) during which the first *k*-space segment was repeatedly sampled to produce a low-resolution series with 330 images, $I_{TA}(x,y,n)$ with $0 \leq n \leq 329$. At the end of the TA period the average cardiac cycle length, RR_{ave}, was calculated from the ECG trigger time stamps. Based on the time stamp stored with each image, each of the 330 low-resolution images acquired during the TA period were mapped to the nearest corresponding cardiac phase, $\hat{n}$, from 20 cardiac phase positions spaced equally throughout a time interval spanning RR_{ave} ($0 \leq \hat{n} \leq 19$). Next, 300 potential

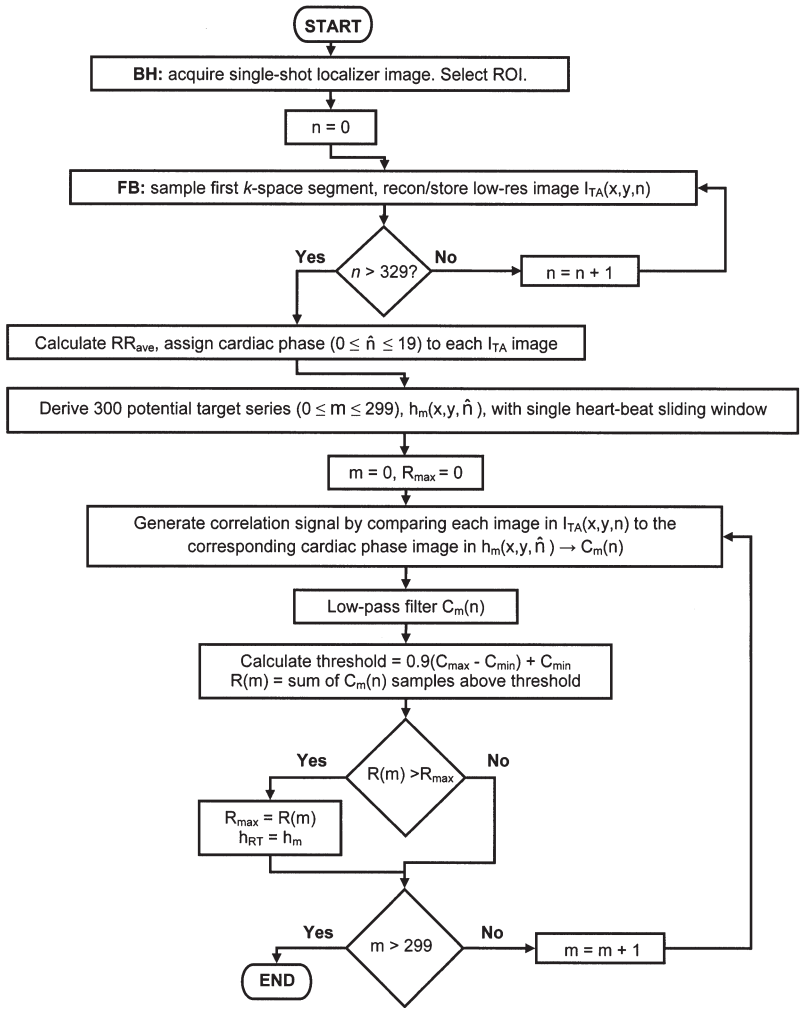

FIG. 1. Flow chart graphically describing the procedural steps for deriving the cardiac phase dependent respiratory target image series.

respiratory target image series were generated, $h_m(x,y,\hat{n})$ with $0 \leq m \leq 299$. Each h_m image set was derived from a sequential subset of I_{TA} using a single heartbeat sliding-window scheme (RR_{ave} temporal aperture). Only 300 potential target image series were produced from the 330 image I_{TA} series because the sliding window generating the h_m series would eventually overrun the end of the I_{TA} series. Although the particular value of m corresponding to I_{TA} series sliding window overrun varies with heart rate, a conservative maximum value of 300 was chosen to eliminate the possibility of overrun even with relatively slow heart rates.

With this temporal aperture several of the 20 cardiac phases for each h_m may not be sampled because the low-resolution image acquisition rate was only 16 frames/s. When necessary, the images for the missing phases were generated by simply setting the image function of the missing cardiac phase equal to that of the nearest sampled phase within the same h_m target series.

The remainder of this derivation strategy relies on (a) the assumption that at least one of the 300 h_m potential target image series was acquired with negligible respiratory motion and at expiration and (b) the assumption that the most frequent and consistent heart position during the TA period corresponded to expiration. These assumptions will be utilized to select which h_m series will be chosen as the respiratory target image series, h_{RT}, and subsequently used for correlation comparison to low-resolution images acquired during the remainder of the free-breathing acquisition.

First, each of the 300 h_m image sets were used to create 300 separate correlation signals, $C_m(n)$, by computing the 2D correlation coefficient between the ROI in each $I_{TA}(x,y,n)$ image and the ROI of the image from h_m with corresponding cardiac phase, $\hat{n}$, for $0 \leq n \leq 329$.

Because the I_{TA} image series is acquired asynchronously to the cardiac cycle, each $C_m(n)$ function may contain cardiac cycle-related artifacts resulting from the correlation comparison of low-resolution images acquired at slightly different cardiac phase position during different heartbeats. Each $C_m(n)$ may also contain high-frequency noise unrelated to respiration. To suppress these artifacts, each $C_m(n)$ signal was low-pass filtered with a 38^{th}-order FIR filter. The coefficients for the filter were derived using the Remez exchange algorithm with design inputs of a transition band from 0.25 to 0.75 Hz, a desired response [1.0, 0.0] and weights [1.0, 1.818] (19). Two example C_m signals (postfiltering) derived using h_m sets acquired at expiration and inspiration are shown in Fig. 2.

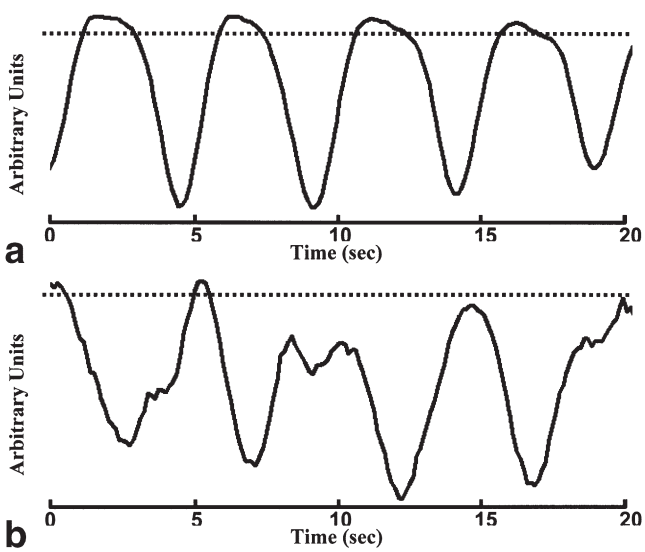

FIG. 2. Example correlation signals derived using target mask series acquired at expiration (**a**) and inspiration (**b**) along with corresponding $0.9(C_{max} - C_{min}) + C_{min}$ thresholds (dashed lines). Notice that the proportion of C_A above threshold, R(a), is much greater than the proportion of C_B above threshold, R(b).

For each of the 300 $C_m(n)$ signals generated, the minimum, C_{min}, and maximum, C_{max}, were determined and the total number of $C_m(n)$ samples above the threshold $0.9(C_{max} - C_{min}) + C_{min,}$ $R(m)$, was recorded for each particular h_m set. The corresponding thresholds from the h_m sets acquired at expiration and inspiration are also shown in Fig. 2. Based on the previously stated assumptions, the h_m set acquired nearest the expiratory phase of the respiratory cycle is expected to produce a C_m signal with a greater $R(m)$ and therefore the h_m set with greatest $R(m)$ was chosen as the final cardiac phase-dependent respiratory target image series, h_{RT}.

Acquisition of Respiratory Self-Gated Cine Imaging Data

Following the TA period, the segmented cine imaging data were acquired. As during the TA period, low-resolution images continued to be reconstructed in real time at 16 frames/s. The 2D correlation between each current low-resolution image and the corresponding cardiac phase of h_{RT} was calculated. The respiratory self-gating signal, $C(n)$, generated by these time series of correlation comparisons was low-pass filtered with the previously described FIR filter. Each of the 40 views included in a single low-resolution image were assigned the same correlation coefficient value. The acquisition respiratory threshold, ART, was chosen as the $0.9(C_{max} - C_{min}) + C_{min}$ value from the TA $C_m(n)$ signal corresponding to h_{RT}.

The acquisition of each segment was halted following the sampling of at least 36 views (90% of each 40 view segment) above the ART threshold at each of 25 cardiac phases (40 ms reconstructed temporal resolution at 60 bpm heart rate). The cardiac phase positions were spaced equally throughout a time interval spanning RR_{ave} and a view-sharing window of 80 ms allowed a single acquired view to be shared between neighboring cardiac phases. The selection of an 80-ms view-sharing window, while acquiring 40 views/segment (120 ms for the acquisition of each 40 view segment) required that each segment be sampled over multiple cardiac cycles in order to provide the necessary views for each cardiac phase.

Initially following completion of the acquisition, the raw data for reconstruction of images at each cardiac phase was selected based on ART criteria as well as the 80 ms cardiac phase inclusion window. If multiple views at the same k-space position were acquired fulfilling the same criteria, the views were linearly weighted based on temporal proximity to the particular cardiac phase position and combined to produce a composite view for inclusion in the final reconstruction. These first few schemes would result in the derivation of at least 90% of the views required for reconstruction at each cardiac phase. The remaining views were derived by first incrementally increasing the cardiac phase view-sharing window time to 100 ms and next by incrementally decreasing the respiratory threshold. Following derivation of the full raw data sets at each of the 25 cardiac phases, the previously described algorithms were used for the final image reconstruction.

Volunteer Studies

Eight healthy volunteers ($N = 8$; 5 male, 3 female) were imaged in mid-cardiac short-axis and long-axis (four-chamber) orientations while breath-holding and while free-breathing. For the breath-hold examinations, only cardiac gating criteria were considered (ART prospectively set to zero and no "target acquisition period") and therefore the breath-hold durations were typically less than 15 s. The previously described imaging parameters were used for both the breath-held and free-breathing acquisitions for optimal comparison purposes. For the free-breathing scans, in addition to the respiratory self- gated image series, image series were reconstructed from the same raw data set, including all of the acquired data (ART retrospectively set to zero) to provide an initial comparison to simple k-space averaging techniques. Therefore, for each imaging orientation, three images series were reconstructed: breath-hold (BH), respiratory self-gating (RSG), and k-space averaging (AVE).

Quantitative Image Sharpness Analysis

The first image in each series was chosen for comparison of myocardium edge sharpness. Bilinear interpolation was used to increase (factor of 6) the number of pixels in the horizontal and vertical dimensions from 192 to 1152. For each image, using MATLAB software (The Mathworks, Inc., Natick, MA), an intensity profile was measured across the septum to left ventricle blood pool boundary, Fig. 3. The local maximum and minimum intensity values across the profile boundary were determined, I_{max} and I_{min}, which corresponded to blood pool and myocardium pixel intensities respectively. Next, the distance, d, between $0.80(I_{max} - I_{min}) + I_{min}$ and $0.2(I_{max} - I_{min}) + I_{min}$ across the profile was measured and the sharpness value for that particular image reported as $1/d$ mm^{-1}. The sharpness quantization strategy was similar to that used by Shea et al. (20) for vessel sharpness scoring of coronary MRA tech-

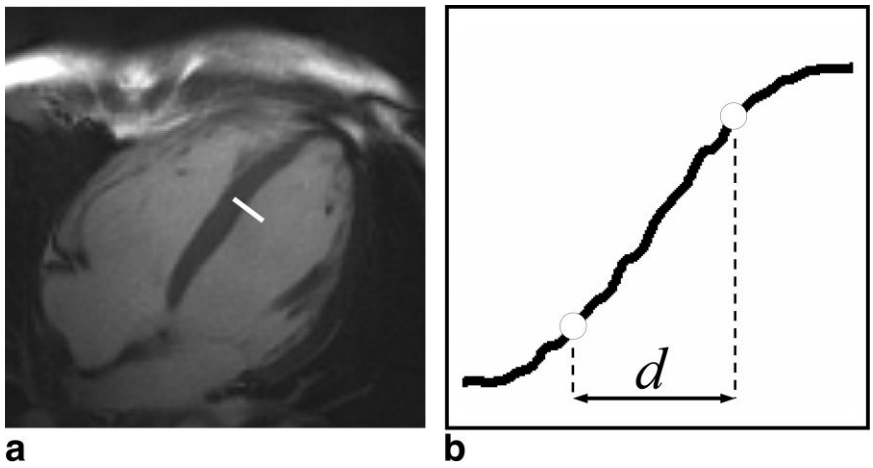

FIG. 3. Example line drawn across the septum to left ventricle blood pool boundary (**a**) used to generate a profile for assessment of edge sharpness (**b**). Open circles represent the 20% and 80% positions between the maximum and minimum intensity values of the profile.

niques. Intensity profiles from images of corresponding free-breathing and breath-held acquisitions were measured at identical positions.

Qualitative Cine Image Series Analysis

Each cine image series was recorded as an image stack such that each could be replayed as a cine loop (25 frames/s) using the Scion Image (Scion Corp., Frederick, MD) software package. For each imaged slice, the cine loops reconstructed using each of the three techniques, BH, RSG, and AVE, were combined into a horizontal 3-on-1 display. Placement within the 3-on-1 display was randomized, and all 3 cine series were simultaneously and synchronously displayed dynamically as cine loops. Two independent reviewers, both cardiac MRI specialists, independently assigned each image series an absolute score for sharpness of definition of fine anatomic structures from 1 (poor) to 4 (excellent) using the following scoring system: 1 = poor definition of anatomic structures with blurring precluding structure visualization, 2 = adequate overall definition of fine anatomic structures sufficient for interpretation, 3 = good overall definition of fine anatomic structures, 4 = excellent overall definition of fine anatomic structures. This qualitative image scoring system was similar to that used by White et al. in previous work describing wireless ECG gating techniques (21). Additionally, to assess subtle differences between the techniques, each cine loop was assigned a sharpness rank (1 = best, 3 = worst) relative to the others within each 3-on-1 display.

RESULTS

Respiratory Self-Gating Signals

A representative correlation coefficient respiratory self-gating signal, $C(n)$, before and after FIR low-pass filtering, is shown in Fig. 4. Notice the suppression of signal modulations due to cardiac cycle related artifacts and high-frequency noise and artifacts unrelated to respiration.

Acquisition Times and Respiratory Scan Efficiency

The BH acquisitions required scan times of 14.8 ± 3.4 s. The free-breathing RSG acquisitions required overall scan times of 76.4 ± 16.6 s, with short-axis and long-axis acquisitions requiring scan times of 72.0 ± 15.7 s and 80.9 ± 17.3 s respectively. These reported scan times do not include the 20 s "target-acquisition" period. Overall respiratory scan efficiency for the RSG technique was 21.8 ± 5.6%, whereas short-axis and long-axis scan efficiencies were 21.1 ± 3.6% and 21.4 ± 4.6% respectively. The differences between the mean scan time in both orientations and scan efficiency in both orientations were not statistically significant.

Respiratory Self-Gated Cine Images

Representative end-diastolic and end-systolic short-axis and long-axis images acquired while breath-holding and free-breathing reconstructed with *k*-space averaging and respiratory self-gating are shown in Figs. 5 and 6, short-axis and long-axis respectively. Notice the blurring of fine anatomic structures (papillary musculature and myocardial trabeculations) in the *k*-space averaging images and the relatively indistinguishable image quality provided by the breath-held and respiratory self-gated images.

Quantitative Cine Image Series Analysis

The mean quantitative image sharpness scores for both short-axis and long-axis imaging orientations are shown in Table 1. One-way ANOVA with Tukey post hoc analysis revealed that the differences between the mean scores of the BH images and mean scores of the free-breathing AVE images were statistically significant as were the differences between the mean scores of the free-breathing AVE images and RSG images ($P < 0.05$). Differences between the mean scores of the BH images and the mean scores of the RSG images were not statistically significant.

Qualitative Cine Image Series Analysis

The mean qualitative image sharpness scores for reviewers 1 and 2 are also shown in Table 1. One-way ANOVA with Tukey post hoc analysis was used for the determination of statistically significant differences ($P < 0.05$) between the qualitative absolute image sharpness scores for each technique. For both reviewers, there were no significant differ-

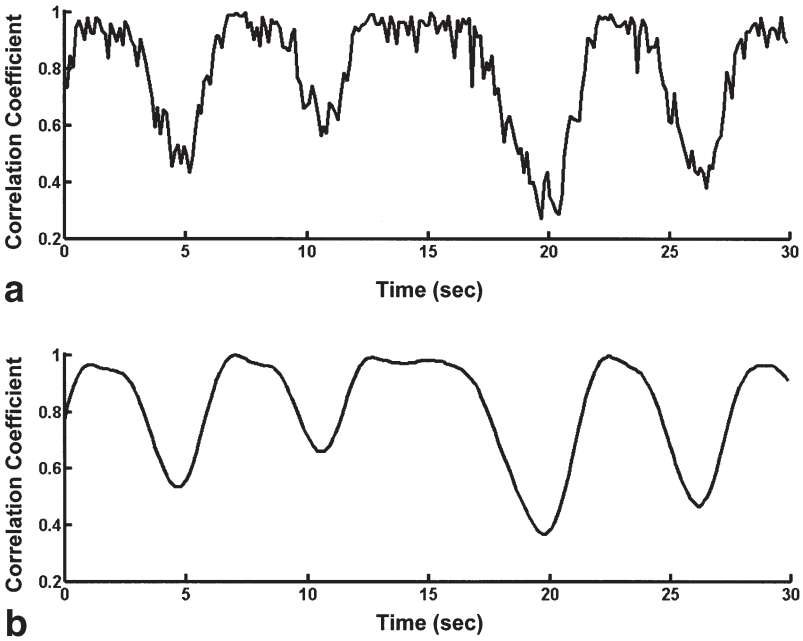

FIG. 4. Representative correlation coefficient respiratory self-gating signal before (**a**) and after (**b**) application of FIR low-pass filter. Notice the suppression of noise and cardiac cycle related signal artifacts.

ences between image sharpness scores of the BH and RSG short-axis image series. For the first reviewer, there was also no significant difference between image sharpness scores of the BH and RSG long-axis image series. For the second reviewer, the long-axis image sharpness scores of the BH image series were significantly higher than the RSG image series. For both reviewers, the image sharpness scores of both the BH image series and RSG image series were significantly higher than the AVE image series in the short-axis and long-axis orientations.

The mean image series ranking scores for each reviewer are also shown in Table 1. For both reviewers, a Friedman nonparametric comparison of ranks provided sufficient evidence to suggest a difference between the mean ranking scores. For both reviewers, Wilcoxon pairwise comparisons revealed the rankings of the AVE image series to be significantly poorer than the rankings of the BH and RSG images series in both long-axis and short-axis orientations. For both reviewers, these pairwise comparisons also revealed the rankings of the BH image series to be significantly better than the RSG image series in the short-axis orientation.

DISCUSSION

A significant portion of the patient population has difficulty performing the necessary breath-holds for conventional segmented cine MRI. Overall image quality (tempo-

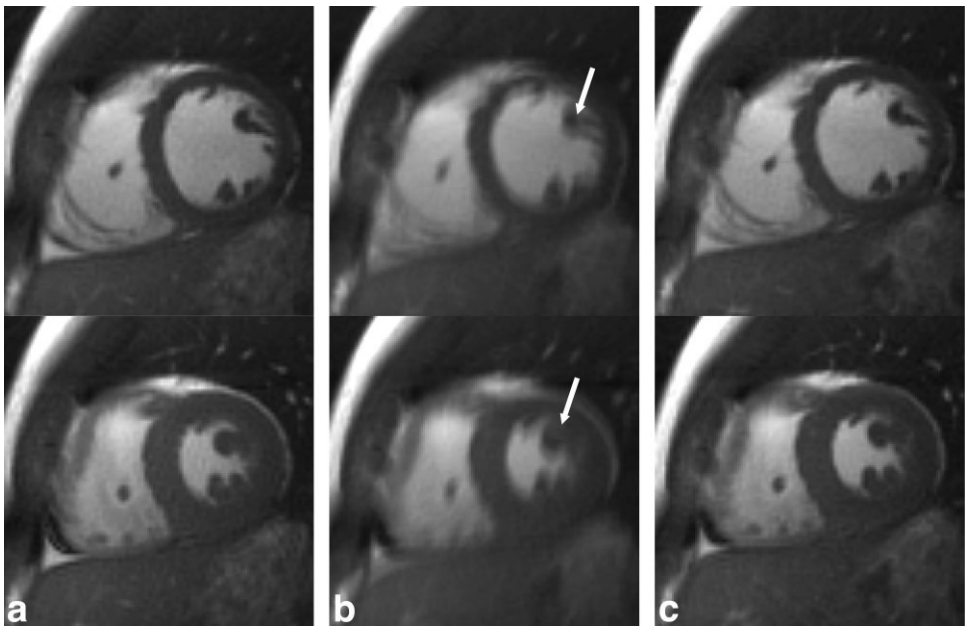

FIG. 5. Representative end-diastole (top row) and end-systole (bottom row) short-axis images from a single volunteer reconstructed from a breath-hold acquisition (**a**) and a free-breathing acquisition with *k*-space averaging (**b**) as well as respiratory self-gating (**c**). Notice the blurring of fine anatomic structures in (**b**), arrows, and the relatively indistinguishable image quality between (a) and (c).

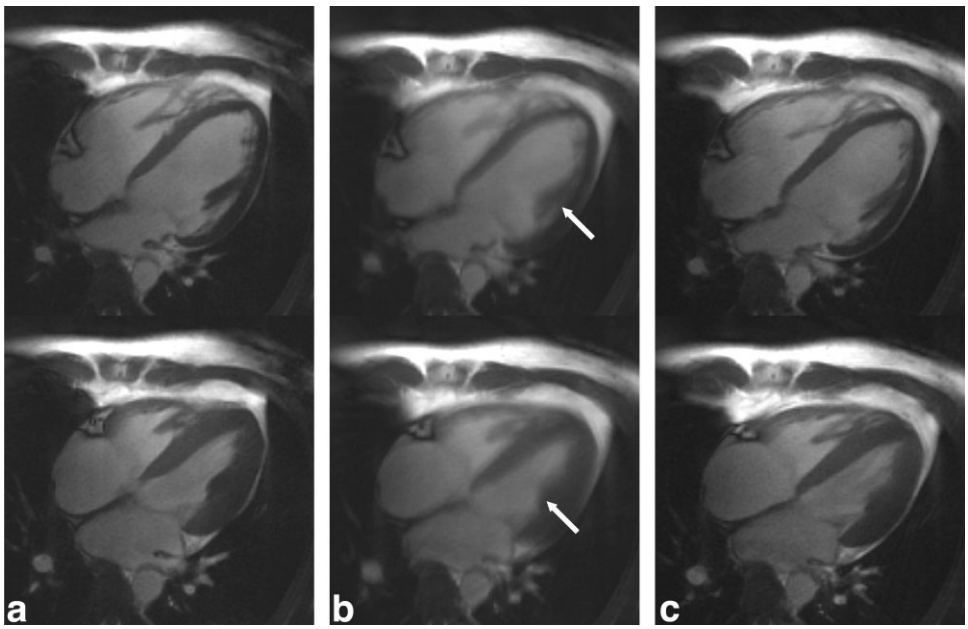

FIG. 6. Representative end-diastole (top row) and end-systole (bottom row) long-axis images from a single volunteer reconstructed from a breath-hold acquisition (**a**) and a free-breathing acquisition with *k*-space averaging (**b**) as well as respiratory self-gating (**c**). Notice the blurring of fine anatomic structures in (b), arrows, and the relatively indistinguishable image quality between (a) and (c).

ral and spatial resolution, SNR, or CNR) could be sacrificed to reduce the breath-hold duration. In this work we present the respiratory self-gating technique as an alternative that does not require such trade-offs, ideally decoupling the choice of relative imaging parameters from breath-hold duration.

A study comparing breath-holding to free-breathing with respiratory self-gating in normal volunteers demonstrated no significant difference in quantitative assessments of image sharpness while respiratory self-gating demonstrated significant improvements over simple *k*-space averaging. With the exception of the long-axis orientation scores for Reviewer 2, comparisons between breath-holding and respiratory self-gating qualitative image sharpness scores demonstrated no significant differences between breath-holding and respiratory self-gating with significant improvements over simple *k*-space averaging in both orientations. However, ranking of image sharpness resulted in statistically significant superior rankings for the breath-hold image series relative to the respiratory self-gated image series. Most of the respiratory self-gated image series exhibited a subtle background temporal intensity variation that was only discernable when replaying each image stack as a cine loop. These resulted from the combination of views at different cardiac phases that were sampled while the imaged tissue was at slightly different positions in the respiratory cycle. Though not affecting the quantitative measures, these subtle intensity variations may have influenced the absolute qualitative scoring or ranking by the reviewers when viewing the series side by side as a dynamic cine display. Future patient studies are necessary to evaluate whether such subtle variations affect the clinical utility of the respiratory self-gating technique.

The overall imaging time required for the free-breathing respiratory self-gated acquisitions were much longer than those required by comparable breath-hold strategies. Even while taking into consideration the recovery time necessary between breath-held acquisitions, such increases in scan time could potentially hinder patient comfort by increasing the overall examination time. To reduce acquisition time, the scan efficiency could potentially be increased by utilizing some of the motion correction techniques already described by Hardy et al. (10,11). Alternatively, a reduction in the total number of views acquired for each image should be possible. In an effort to focus this work on the derivation of gating signals rather than on the salient properties of undersampled projection reconstruction (22,23), we chose to acquire 160 total views/image, effectively 20% less undersampled than previously reported radial TrueFISP segmented cine techniques (13). Decreases of in scan time should be possible

Table 1
Image Sharpness Scores

Technique	Qualitative (units of mm^{-1})		Quantitative (Reviewer 1)		Quantitative (Reviewer 2)	
	Short-axis	Long-axis	Short-axis (absolute/rank)	Long-axis (absolute/rank)	Short-axis (absolute/rank)	Long-axis (absolute/rank)
Breath-hold	0.58 ± 0.13	0.48 ± 0.11	4.00 ± 0.00/1.00 ± 0.00	3.75 ± 0.46/1.13 ± 0.35	3.87 ± 0.35/1.13 ± 0.35	3.87 ± 0.35/1.75 ± 0.71
Free-breathing averaging	0.28 ± 0.04	0.31 ± 0.07	3.00 ± 0.00/2.88 ± 0.35	2.62 ± 0.52/3.00 ± 0.00	1.88 ± 0.35/3.00 ± 0.00	2.00 ± 0.00/2.75 ± 0.71
Free-breathing self-gating	0.55 ± 0.11	0.48 ± 0.09	4.00 ± 0.00/1.50 ± 0.53	3.87 ± 0.35/1.62 ± 0.52	3.63 ± 0.52/1.88 ± 0.35	3.38 ± 0.52/1.50 ± 0.53

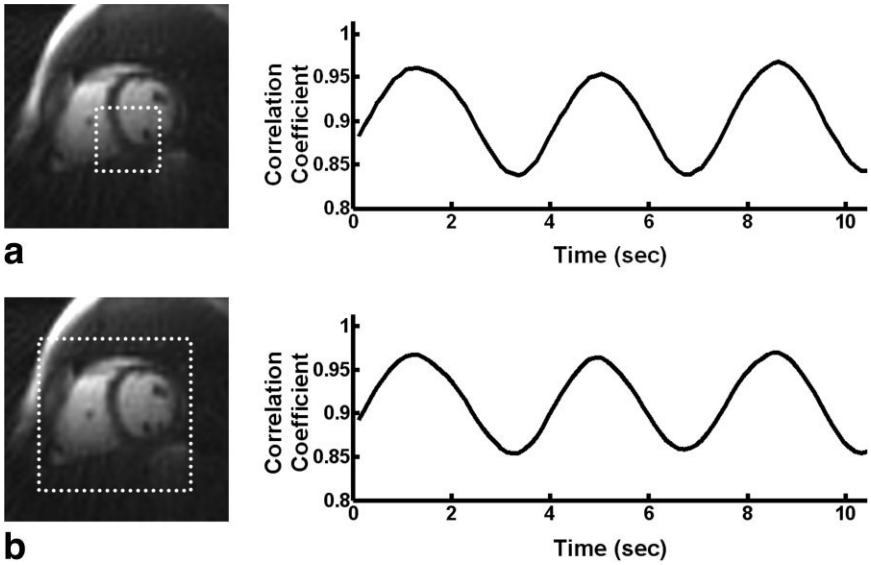

FIG. 7. Comparison between the respiratory self-gating signal derived using a smaller ROI of 50 × 50 mm^2 (**a**) and the respiratory self-gating signal derived using a larger ROI of 120 × 120 mm^2 covering the entire heart (**b**). Notice the similarity between the two signals in this example.

by simply incorporating similar imaging parameters. Small additional decreases in scan time can likely be achieved by reducing the number of dummy pulses applied to achieve steady state prior to data acquisition.

The particular choices of ROI position were based on previous observations of significant blurring in these regions when using averaging techniques while imaging during free-breathing. Although other ROI positions may have sufficed, we chose to use a single position for each orientation to maintain a consistent methodology. An ROI with dimensions smaller than those necessary to cover the entire heart were used for these studies to reduce correlation coefficient computation times allowing near real-time generation of the respiratory gating signal during the acquisition. However, the necessity to manually select a limited ROI, specifically located at an anatomic position sufficiently reflective of respiratory motion, could add undesirable procedural complications if utilizing respiratory self-gating techniques in a clinical setting. Initial off-line postprocessing investigations of simply using a much larger ROI covering the entire heart for respiratory self-gating have demonstrated that such a strategy produces gating signals very similar to those produced from a reduced ROI. An example comparing the self-gating signal produced using a smaller ROI (50 × 50 mm^2) and larger ROI covering the entire heart (120 × 120 mm^2) are shown in Fig. 7. However, more rigorous studies are necessary to confirm that the larger ROI strategy continues to produce signals sufficient for respiratory gating. Provided that sufficient gating signals can be produced and that algorithms and software can be improved to handle the added computational requirements necessary using a larger ROI, such a strategy could significantly reduce procedural burdens when utilizing the respiratory self-gating techniques.

The choice of 20 cardiac phases for the respiratory target image series was based on the common use of 15 to 20 cardiac phases for conventional cine imaging. Further investigations into optimum ROI choice in different imaging orientations and the optimum number of target cardiac phases could provide improvements to the respiratory self-gating technique.

For this initial respiratory self-gating work, low-resolution gating images were reconstructed as opposed to full-resolution gating images, including all 192 sampled readout points for each view. Reconstruction of full-resolution gating images would have resulted in significant undersampling streak artifact. The position of these artifacts would change according to the particular *k*-space segment sampled and thereby compromise the correlation comparisons between images reconstructed from imaging data acquired at different *k*-space segments. Intuitively, one might expect that the use of these lower resolution images for gating signal derivation might result in an inability to detect in-plane rigid displacements of distances smaller than the low-resolution image voxel dimensions. However, as rigorously described by Sussman et al. (12,24) who refers to the work of Hajnal et al. (25), image resolution is actually not a limiting factor given sufficient image SNR. However, future studies are certainly necessary to determine (a) the minimum displacement discernable with the RSG technique given the use of a relatively high SNR TrueFISP pulse sequence implementation and (b) the optimal gating image spatial and temporal resolution for free-breathing cine MRI, particularly to measure displacement for motion correction.

Previous work has described the development of image correlation, complex echo-peak and center-of-mass (COM) cardiac self-gating strategies for "wire-less" segmented cine MRI (9). Although each of these self-gating strategies can provide respiratory gating information, we chose the correlation approach for this initial feasibility study because it provides a gating signal derived from 2D image space, thereby avoiding corruption of the respiratory gating signal by tissues external to the selected ROI. Image-domain correlation-based approaches can provide respiratory gating information based on changes in the position of the heart rather than remote changes in diaphragm or chest wall position. This property should be useful while imaging free-breathing patients exhibiting erratic respiratory patterns; however, further comparison studies with bellows and NAV echo techniques are still necessary. The cardiac self-gating strategies can be combined with the

respiratory self-gating strategy described by this work to allow free-breathing segmented cine MRI without the need for ECG triggering (26). However, previous work combining the self-gating strategies utilized only retrospective respiratory gating, potentially much less efficient than the prospective respiratory gating approach described by this work. Furthermore, the accuracy of self-gated cardiac cycle synchronization during free-breathing has yet to be established. Ideally for combined cardiac and prospective respiratory self-gating, efficient signal processing techniques are necessary to allow real-time separation of the respiratory and cardiac gating signal components and real-time detection of cardiac phase and respiratory position based on these signals.

Although rigorous clinical validation of the respiratory self-gating technique has not been performed, wall motion abnormalities should not pose any complications for respiratory self-gating provided that heart motion remains constant relative to respiratory cycle position. However, particularly because of the long overall acquisition times for the respiratory self-gating scans, arrhythmias producing intermittent changes in cardiac motion could certainly pose problems for the proposed gating signal derivation strategy. Further investigations are necessary to evaluate the sensitivity of the respiratory self-gating technique to intermittent changes in cardiac motion patterns.

Derivation of the respiratory target image series, h_{RT}, based on the target acquisition strategy proposed by this work, relies on an assumption that the h_m set generated at expiration will produce a correlation signal, $C_m(n)$, having the greatest number samples above $0.9(C_{max} - C_{min}) + C_{min}$. Although successful for these initial feasibility studies, such an assumption may not always hold. In these cases it may be necessary to include additional information for the derivation of the respiratory target image series, potentially provided by a COM signal derived from the same raw data (26). Alternatively, a hybrid approach could be used that incorporates a single-heartbeat breath-hold to derive h_{RT} (10,11). Derivation of a gating signal representative of respiration depends on adequate respiratory motion within the chosen ROI. For this preliminary study, we investigated imaging in only two common cardiac cine imaging orientations. Furthermore, the duration of the target acquisition period was empirically chosen (20 s to sample 330 low-resolution images) based on initial failures of the strategy when using shorter durations of only 10 s. Further studies are necessary to optimize target acquisition duration and evaluate the respiratory self-gating technique in all clinically important orientations.

Parallel imaging techniques can allow significant reductions in breath-hold lengths for segmented cine MRI (27–29) while continuing to provide sufficient spatial resolution, temporal resolution, and overall image quality. These accelerated imaging strategies may be sufficient to image patients who cannot maintain the breath-holds necessary for conventional segmented cine techniques. However, the continued necessity for even a very short breath-hold remains problematic for some patients. Future studies are needed to determine if parallel imaging techniques, free-breathing respiratory gating techniques as described by this work, or some combination provide the best practical solution for imaging patients having difficulties breath-holding.

CONCLUSIONS

This work described the respiratory self-gating technique and in vivo experiments demonstrated the feasibility of using the technique to acquire high-temporal-resolution and high-spatial-resolution cine images while free-breathing. For this initial study, the respiratory self-gating technique was able to produce cine series with no significant differences in quantitative image sharpness scores to image series produced using comparable breath-held segmented cine techniques. Because of the common difficulties associated with breath-holding, respiratory gating techniques that permit segmented *k*-space acquisition while free-breathing represent important practical advances for clinical cardiac MRI.

ACKNOWLEDGMENTS

The authors thank Dr. Daniel Herzka from the NIH NHLBI Laboratory of Cardiac Energetics for the development of the MATLAB image-processing tools utilized by this work.

REFERENCES

1. Runge VM, Clanton JA, Partain CL, James AEJ. Respiratory gating in magnetic resonance imaging at 0.5 Tesla. Radiology 1984;151:521–523.
2. Bailes D, Gilderdale D, Bydder G, Collins A, Firmin D. Respiratory ordered phase encoding (ROPE): a method for reducing respiratory motion artifacts in MR imaging. J Comput Assist Tomogr 1985;9:835–838.
3. Yuan Y, Axel L, Hernandez E, Dougherty L, Pilla J, Scott C, Ferrari V, Blom A. Cardiac-respiratory gating method for magnetic resonance imaging of the heart. Magn Res Med 2000;43:314–318.
4. Korin HW, Ehman RL, Riederer SJ, Felmlee JP, Grimm RC. Respiratory kinematics of the upper abdominal organs: a quantitative study. Magn Reson Med 1992;23:172–178.
5. Li D, Kaushikkar S, Haacke EM, Woodard PK, Dhawale P, Kroeker RM, Laub G, Kuginuki Y, Gutierrez FR. Coronary arteries: three-dimensional MR imaging with retrospective respiratory gating. Radiology 1996;201:857–863.
6. Oshinski JN, Hofland L, Mukundan S, Dixon WT, Parks WJ, Pettigrew RI. Two-dimensional coronary MR angiography without breath holding. Radiology 1996;201:737–743.
7. McConnell MV, Khasgiwala VC, Savord BJ, Chen MH, Chuang RR, Edelman RR, Manning WJ. Prospective adaptive navigator correction for breath-hold MR coronary angiography. Magn Reson Med 1997;37:148–152.
8. Carr J, Simonetti O, Bundy J, Li D, Pereles S, Finn J. Cine MR angiography of the heart with segmented true fast imaging with steady-state precession. Radiology 2001;219:828–834.
9. Larson A, White R, Laub G, McVeigh E, Li D, Simonetti O. Self-gated cardiac cine MRI. Magn Res Med 2004;51:93–102.
10. Hardy C, Zhao L, Zong X, Saranathan M, Yucel E. Coronary MR angiography: respiratory motion correction with BACSPIN. J Magn Reson Imag 2003;17:170–176.
11. Hardy C, Saranathan M, Zhu Y, Darrow R. Coronary angiography by real-time MRI with adaptive averaging. Magn Reson Med 2000;44:940–946.
12. Sussman MS, Stainsby JA, Robert N, Merchant N, Wright GA. Variable-density adaptive imaging for high-resolution coronary artery MRI. Magn Reson Med 2002;48:753–764.
13. Shankaranarayanan A, Simonetti O, Laub G, Lewin J, Duerk J. Segmented k-space and real time cardiac cine using radial trajectories. Radiology 2001;221:827–836.

14. Deimling M, Heid O. Magnetization prepared trueFISP imaging. In: Proceedings of SMRM, San Francisco, CA; 1994. p 495.
15. Jackson J, Meyer C, Nishimura D. Selection of a convolution function for Fourier inversion using gridding. IEEE Trans Med Imag 1991;10: 473–478.
16. Joseph P. Sampling errors in projection reconstruction MRI. Magn Res Med 1998;40:460–466.
17. Dale B, Wendt M, Duerk J. A rapid look-up table method for reconstructing MR images from arbitrary *k*-space trajectories. IEEE Trans Med Imag 2001;20:207–217.
18. Roemer P, Edelstein W, Hayes C, Souza S, Meuller O. The NMR phased array. Magn Res Med 1990;16:192–225.
19. Oppenheim A, Schafer R. Discrete-time signal processing. Upper Saddle River, NJ: Prentice Hall; 1999.
20. Shea S, Kroeker R, Deshpande V, Laub G, Zheng J, Finn J, Li D. Coronary artery imaging: 3D segmented k-space data acquisition with multiple breath-holds and real-time slab following. J Magn Reson Imaging 2001;13:301–307.
21. White R, Paschal C, Clampitt M, Spraggins T, Lenz G. Electrocardiograph-independent "wireless" cardiovascular cine MR imaging. J Magn Reson Imag 1991;1:347–355.
22. Scheffler K, Hennig J. Reduced circular field-of-view imaging. Magn Reson Med 1998;40:474–480.
23. Peters D, Korosec F, Grist T, Block W, Holden J, Vigen K, Mistretta C. Undersampled projection reconstruction applied to MR angiography. Magn Res Med 2000;43:91–101.
24. Sussman MS, Wright GA. Factors affecting the correlation coefficient template matching algorithm with application to real-time 2-D coronary artery MR imaging. IEEE Trans Med Imaging 2003;22:206–216.
25. Hajnal JV, Saeed N, Soar EJ, Oatridge A, Young IR, Bydder GM. A registration and interpolation procedure for subvoxel matching of serially acquired MR images. J Comput Assist Tomogr 1995;19:289–296.
26. Larson A, Simonetti O, White R, Laub G, McVeigh E. Cardiac and respiratory self-gated projection reconstruction cine imaging. In: Proceedings of the 89th Scientific Assembly and Annual Meeting, RSNA, Chicago, IL. 2003. p 591.
27. Sodickson D, Manning W. Simultaneous acquisition of spatial harmonics (SMASH)-fast imaging with radiofrequency coil arrays. Magn Reson Med 1997;38:591–603.
28. Pruessmann K, Weiger M, Scheidegger M, Boesiger P. SENSE: sensitivity encoding for fast MRI. Magn Reson Med 1999;42:952–962.
29. Griswold MA, Jakob PM, Heidemann RM, Nittka M, Jellus V, Wang J, Kiefer B, Haase A. Generalized autocalibrating partially parallel acquisitions (GRAPPA). Magn Reson Med 2002;47:1202–1210.